Emergence of ferromagnetism through the metal-insulator transition in undoped indium tin oxide films

Samuel Mumford [1,2,*,†] Tiffany Paul [1,3,*] and Aharon Kapitulnik [1,2,3]

[1]*Geballe Laboratory for Advanced Materials, Stanford University, Stanford, California 94305, USA*
[2]*Department of Physics, Stanford University, Stanford, California 94305, USA*
[3]*Department of Applied Physics, Stanford University, Stanford, California 94305, USA*

We present a detailed study of the emergence of bulk ferromagnetism in low-carrier-density samples of undoped indium tin oxide. We use annealing to increase the density of oxygen vacancies and change the sample morphology without introducing impurities through the metal insulator transition (MIT). We utilize a novel and highly sensitive "Corbino-disk torque magnetometry" technique to simultaneously measure the thermodynamic and transport effects of magnetism on the same sample after successive annealing. With increased sample granularity, the carrier density increases, the sample becomes more metallic, and ferromagnetism appears as the resistance approaches the MIT. Ferromagnetism is observed through the detection of magnetization hysteresis, the anomalous Hall effect (AHE), and hysteretic magnetoresistance. A sign change of the AHE as the MIT is approached may elucidate the interplay between the impurity band and the conduction band on the weakly insulating side of the MIT.

I. INTRODUCTION

The initial discovery of room-temperature ferromagnetism in Co-doped TiO_2 [1] films was soon followed by the observation of similar behavior in other transition-metal (TM) doped oxides including Co-doped SnO_2 [2], Mn-doped ZnO [3], Co-doped CeO_2 [4], and Ni, Mo, Fe, and Mn-doped In_2O_3 [5–8]. The origin of the observed thin-film magnetism continues to be debated, particularly after the discovery of ferromagnetism in undoped oxides such as HfO_2 [9], TiO_2, and In_2O_3 [10]. At the heart of the puzzle is the observation that the respective bulk undoped oxides exhibit only diamagnetism. Similarly, the doping level in TM doped oxides was often too low to explain the observed strength, anisotropy, or thermal treatment sensitivity of the magnetic state. Correlation between the samples' morphology and the occurrence of magnetism instead suggests an explanation based on the spontaneous formation of defects or oxygen vacancies [10]. The abundant surface vacancies of the nanoparticles which make up a granular structure provide unpaired electron spins which could interact via an exchange mechanism [11].

With the observation of ferromagnetism in In_2O_3 and SnO_2, it is natural to explore whether the widely used solid solution of tin-doped indium oxide (ITO) exhibits ferromagnetism. Ferromagnetism could be used to integrate this optoelectronic material into novel spintronics applications. Indeed, various TM doped [6,12–15] and undoped [5,16,17] ITO systems were shown to exhibit ferromagnetism that persisted to room temperature. Oxygen vacancy defects have been proposed as the source of magnetic moments rather

than impurities [17–19], while itinerant carriers mediate the collective ferromagnetic state [15,16,20]. A persistent obstacle in proclaiming intrinsic ferromagnetism for ITO has been the difficulty in observing the anomalous Hall effect (AHE) and hysteretic magnetoresistance. For example, in Cr-doped ITO the AHE appears only at very high carrier concentrations, exceeding 10^{21} cm^{-3} [15], while in 12% Co-doped ITO (10% Sn) the AHE appears above $\sim 10^{19}$ cm^{-3}. Samples of ITO with lower concentrations of magnetic elements generally do not show the AHE, and the observed negative magnetoresistance is attributed to a magnetic-field-induced reduction in spin scattering [15,19,20]. Similar to other magnetic semiconductors (e.g., [21]), ITO is a heavily doped *n*-type semiconductor typically studied near the metal-insulator transition (MIT). In particular, undoped ITO close to the MIT may exhibit local magnetic moments that are typically self-generated in quenched disordered electronic systems due to interaction effects [22]. Thus the carrier density may not be the only relevant parameter for magnetism [20,23]. It is correspondingly important to elucidate the occurrence of ferromagnetism in undoped ITO within these contexts.

In this work we examine the interplay between morphology, proximity to the MIT, and the emergence of bulk magnetic properties in low-carrier-density samples of ITO. We used annealing to increase the density of oxygen vacancies and change the sample granularity without introducing impurities [24–31]. Annealing reduced the resistivity and was performed across the MIT. We utilized a novel and highly sensitive *Corbino disk torque magnetometry* technique to simultaneously measure the thermodynamic and transport effects of magnetism on the same sample after successive annealing. Our results clearly show the following. (i) Starting with a highly insulating, mostly amorphous ITO with no observed magnetism, successive annealing induces morphology

---

*These authors contributed equally to this article.
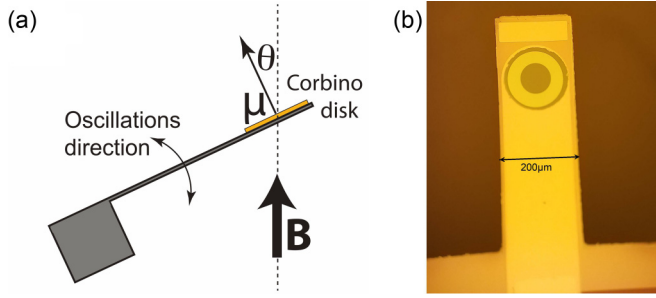†smumfor2@stanford.edu

FIG. 1. (a) Schematic of torque magnetometry where Hall currents in a Corbino disk induce the magnetic moment μ; adapted from [32]. (b) Picture of the ITO Corbino disk cantilever. The center contact is connected to an underlying ground plane. The metal pad on the end of the cantilever is used for optical alignment.

change towards a more granular structure. This change is accompanied by an increase in the carrier density and occurrence of ferromagnetism near the MIT. (ii) The amplitude of magnetization hysteresis and saturating field both increase with decreased sheet resistance, indicating strengthening of the ferromagnetic state. (iii) Undoped ITO thus is ferromagnetic, exhibiting the anomalous Hall effect and hysteretic magnetoresistance for a carrier density as low as $\approx 3 \times 10^{18}$ carriers/cm^3. (iv) Both the AHE and hysteretic magnetoresistance are observed across the MIT. The sign of the AHE changes from negative on the insulating side of the MIT to positive on the metallic side of the MIT.

II. EXPERIMENT

A. Preparation of samples

Hall bar and Corbino disk patterned ITO samples were prepared by radio-frequency magnetron sputtering using a 10% Sn target at 8 W/in.^{2}, 5 mT of Ar pressure, and 2.5% partial pressure of O$_2$. Both Hall bar and Corbino disk samples were subjected to successive annealing schedules at 400 K and a pressure of $<10^{-5}$ T, with measurements performed after each multiday anneal. A typical ITO sample was initially highly insulating and exhibited a starting sheet resistance of 70 k$\Omega/\square$ at room temperature and a thickness of 40 nm. The resistance increased to 460 k$\Omega/\square$ at the measurement base temperature of 4.2 K. Measurements were performed in a liquid helium cryostat with a 7-T superconducting magnet. Hall effect and magnetoresistance were measured on the Hall bars using the standard five-lead configuration. The Corbino disk samples were measured by torque magnetometry as described below.

B. Corbino disk torque magnetometry

Cantilever torque magnetometry utilizes a high-Q resonator to detect the interaction between a magnetic dipole $\vec{\mu}$ and an external magnetic field $\vec{B}$ [32–36], where the resulting torque is [34]

$$\vec{\tau} = \vec{\mu} \times \vec{B}. \tag{1}$$

A schematic of cantilever torque magnetometry is shown in Fig. 1(a). The angular response θ of a cantilever with moment of inertia A, resonant frequency ω_0, and quality factor Q sub-

ject to an external torque τ may be approximated as a damped harmonic oscillator following [37]

$$A\ddot{\theta} + \frac{A}{Q}\omega_0\dot{\theta} + A\omega_0^2\theta = \tau. \tag{2}$$

The torque of a dipole parallel to the cantilever surface norm and a static z-aligned magnetic field B shifts the resonant frequency as

$$A\omega_0^2 \rightarrow A\omega_0^2 - \mu B \quad \text{or} \quad \frac{\Delta\omega_0}{\omega_0} = \frac{\mu B}{2A\omega_0^2}. \tag{3}$$

The circulating current in a Corbino disk [38] patterned on a cantilever forms such a magnetic dipole parallel to the cantilever surface norm [32]. Silicon cantilevers of dimension $200 \times 600 \times 3$ μm were fabricated with Corbino disks as shown in Fig. 1(b). The resulting devices exhibited $A = 3 \times 10^{-18}$ kg-m^2 and $f_0 = \omega_0/2\pi = 14.616$ kHz. Finally, the cantilever resonant frequency was observed interferometrically and driven through laser radiation pressure [32].

Cantilevers with ITO Corbino disks were examined for magnetization and magnetic transport effects. Sample magnetization is measured through the voltage-independent shift in resonant frequency:

$$\Delta f_0(B) = f_0(B) - f_0(B = 0). \tag{4}$$

Sample transport properties for the Corbino disk voltage V are measured through the voltage-dependent shift

$$\delta f_0(\pm V, B) = f_0(+V, B) - f_0(-V, B). \tag{5}$$

The Hall effect is measured through the even in B component of $\delta f_0(\pm V, B)$, while the odd component of $\delta f_0(\pm V, B)$ is caused by contact misalignment and longitudinal current. As shown by Mumford *et al.* [32], using Eq. (3) the even component of $\delta f_0(\pm V, B)$ yields the Hall conductivity

$$\sigma_{xy} = C\frac{\delta f_0}{BV}, \quad \text{where} \quad C = \frac{4Af_0\ln(r_o/r_i)}{\pi(r_o^2 - r_i^2)} \tag{6}$$

and r_o and r_i are the outer and inner radii of the disk. Thus, $\delta f_0(\pm V, B)$ is proportional to $\sigma_{xy}B$ and the expected Hall contribution to δf_0 is proportional to B^2 for $\sigma_{xy} \propto B$. The quadratic dependence of the even component of $\delta f_0(\pm V, B)$ and the extraction of Hall conductivity for a nonmagnetic sample are shown in Fig. 2.

III. RESULTS AND DISCUSSION

A. Characterization of samples

The ITO grain size and granularity increased with annealing as shown in Fig. 3. As deposited, the ITO was largely amorphous with a smooth surface profiled by atomic force microscopy. After annealing, the ITO subdivided into grains with height fluctuations nearly equal to the deposited ITO thickness as shown in Figs. 3(a) and 3(b). Complimentary scanning electron microscope (SEM) images also demonstrate a change in granularity with annealing. Two samples of ITO were analyzed by SEM. Sample 1 was patterned in a Hall bar [Figs. 3(a) and 3(b)/3(c) and 3(d)] and sample 2 was patterned in a Corbino disk [Figs. 3(e) and 3(f)]. As deposited in a Hall bar, the ITO exhibited an amorphous structure, with
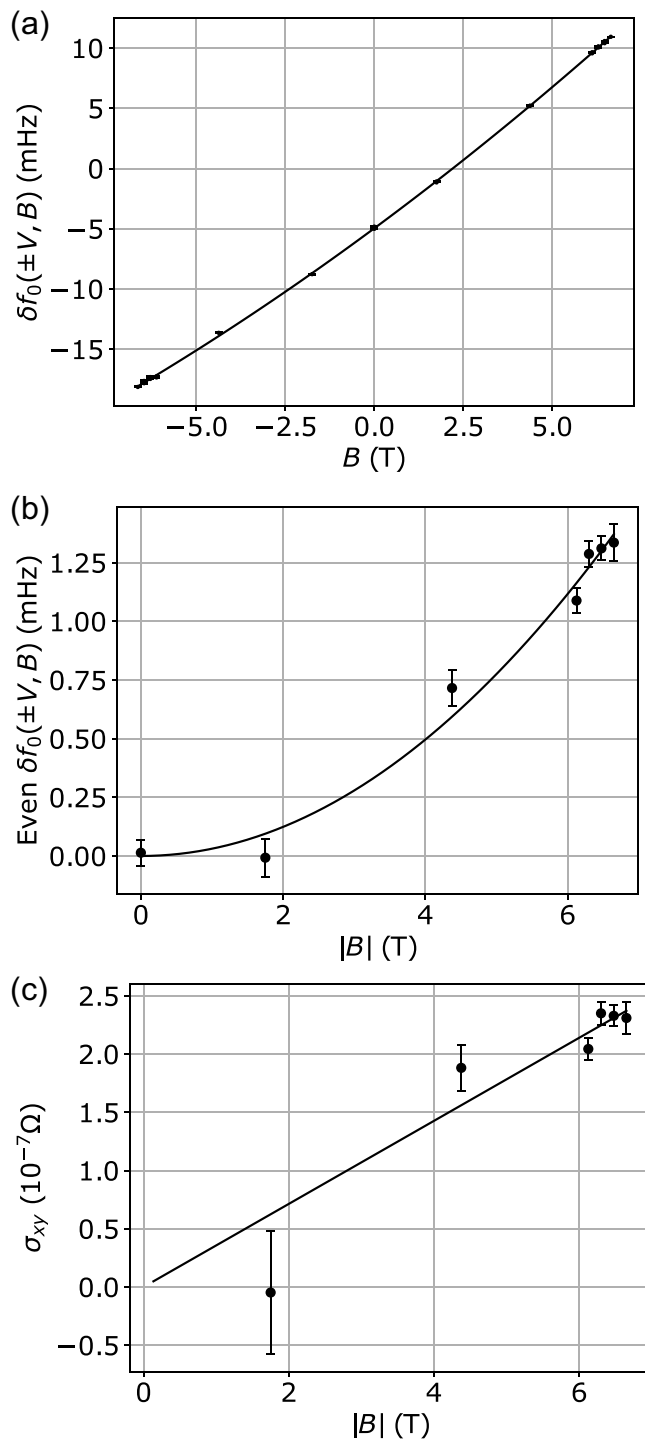
FIG. 2. An example of extracting the even component of $\delta f_0(\pm V, B)$ and σ_{xy} for nonmagnetic metallic ITO; adapted from [32]. (a) A full data set of $\delta f_0(\pm V, B)$ including the linear in B term in $\delta f_0(\pm V, B)$ due to misalignment. (b) The even component of $\delta f_0(\pm V, B)$ found by averaging $\delta f_0(\pm V, -B)$ and $\delta f_0(\pm V, +B)$. (c) Extracted Hall conductivity from the even component of $\delta f_0(\pm V, B)$ and Eq. (6).
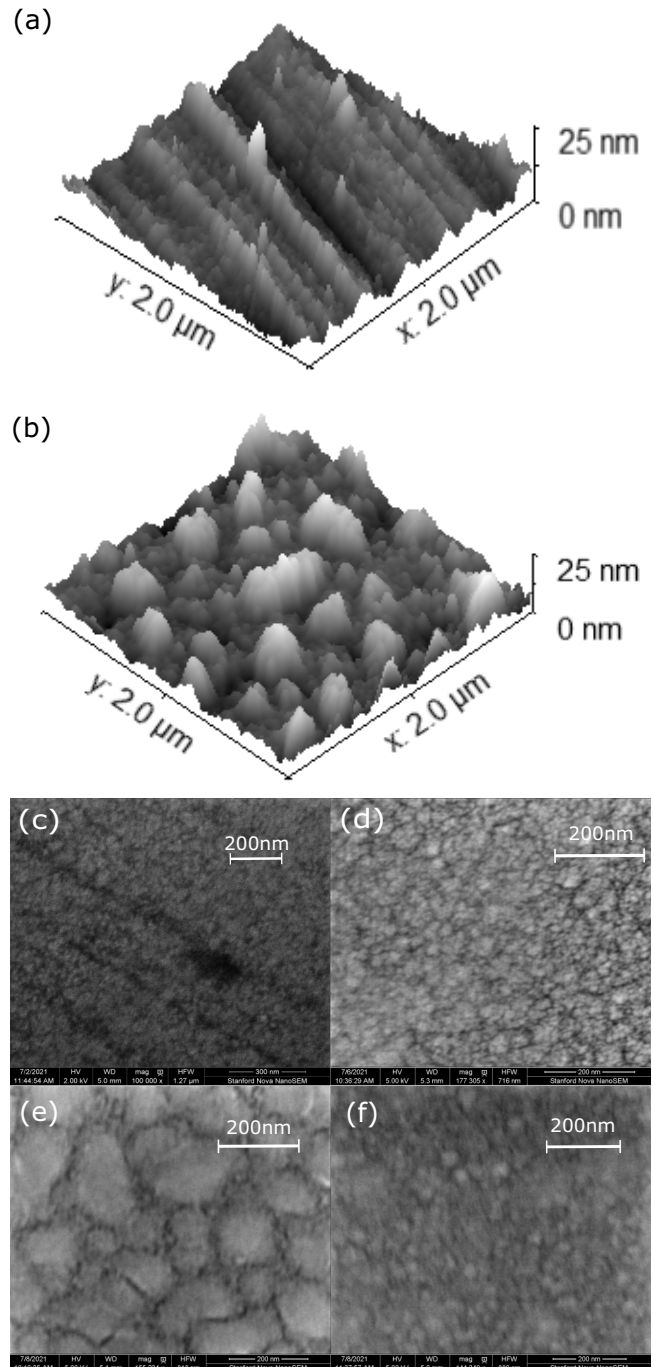

FIG. 3. Characterization of the granularity of ITO with annealing. The initially large patches of ITO or smooth ITO break down into granular areas after annealing. (a, b) Atomic force microscopy profile of the ITO Hall bar before and after annealing. Sample height fluctuations and granularity increase after annealing. (c, d) SEM images of the ITO Hall bar before and after annealing. (e, f) SEM images of the Corbino disk ITO before and after annealing.

only stripes and SEM noise seen in Figs. 3(a) and 3(c). The unannealed Corbino disk ITO shown in Fig. 3(e) instead exhibits large grains. The differences between the as-deposited ITO in the Corbino disk and the Hall bar may be explained by a difference in deposited ITO morphology based on the substrate [39] or by partial annealing of the Corbino disk ITO during cantilever plasma etching. After annealing, the ITO became granular, with a typical grain size of the order of 500 nm^2 in both sample geometries. The convergence of

TABLE I. Samples investigated in this study and their transport properties at base temperature.

Resistivity $(k\Omega/\square)$	Configuration	n $(10^{18}\ cm^{-3})$
3300	Corbino disk	-0.08 ± 0.2
460	Corbino disk	0.17 ± 0.04
185	Corbino disk	1.7 ± 1
48	Corbino disk	3.4 ± 0.5
32	Corbino disk	-2.7 ± 0.3
17	Corbino disk	6.5 ± 1.4
15	Hall bar	9.33 ± 0.02
8.5	Corbino disk	22 ± 10
4.6	Hall bar	23.7 ± 0.1

grain geometries by image grain detection is shown in Fig. 9 in Appendix A. The sheet resistance at base temperature also decreased with annealing, while the carrier density increased as reported in Table I. Such a change in grain size [24–30], decreased resistivity, and increased carrier density [24,26–28,31] are consistent with previous observations of ITO with higher temperature thermal annealing.

B. Corbino disk torque magnetometry of ITO

1. Hall conductivity annealing across the MIT

An initially highly resistive ITO cantilever (resistivity of 3300 kΩ/$\square$ at base temperature) was annealed in six steps to investigate the variation of Hall conductivity through the MIT as well as the onset and evolution of magnetism. Figure 4(a) shows the measured Hall conductivity at 5 T of an ITO sample with annealing, while the respective carrier densities are listed in Table I. Annealed Hall bar configuration samples are included for comparison. Ferromagnetism emerged close to the MIT and thus complicated extracting the ordinary Hall effect from $\delta f_0(\pm V, B)$ as discussed in further detail below. This increased complexity increases the uncertainty in σ_{xy} extracted near and below the MIT, but the observed carrier densities remain consistent with similarly prepared samples measured in a Hall bar configuration.

An important result to be drawn from the high-resistance samples deep in the hopping regime is the tendency of σ_{xy} to vanish with increasing disorder or increasing ρ_{xx}. The hopping regime Hall effect is governed by the self-interference effect of the electron wave function propagating along limited paths dictated by the magnetic field and the impurity sites responsible for the impurity band. Early theoretical work by Friedman and Pollak [40] using the Holstein approach [41] concluded that the Hall resistivity diverges as the temperature tends to 0. This result was then reinforced by Entin-Wohlman *et al.* [42], who attempted to explain the discrepancy with complementary calculations predicting an electronic state where the longitudinal resistance diverges at zero temperature, but the Hall resistivity remains constant [43–45]. Such a state is known as a Hall insulator. Indeed, while experimental results focused in the vicinity of the MIT confirmed divergence of ρ_{xy} on the insulating side [46,47], in other experiments insulating states derived from quantum Hall states were consistent with a Hall insulator. The result for ρ_{xy} may be different depending
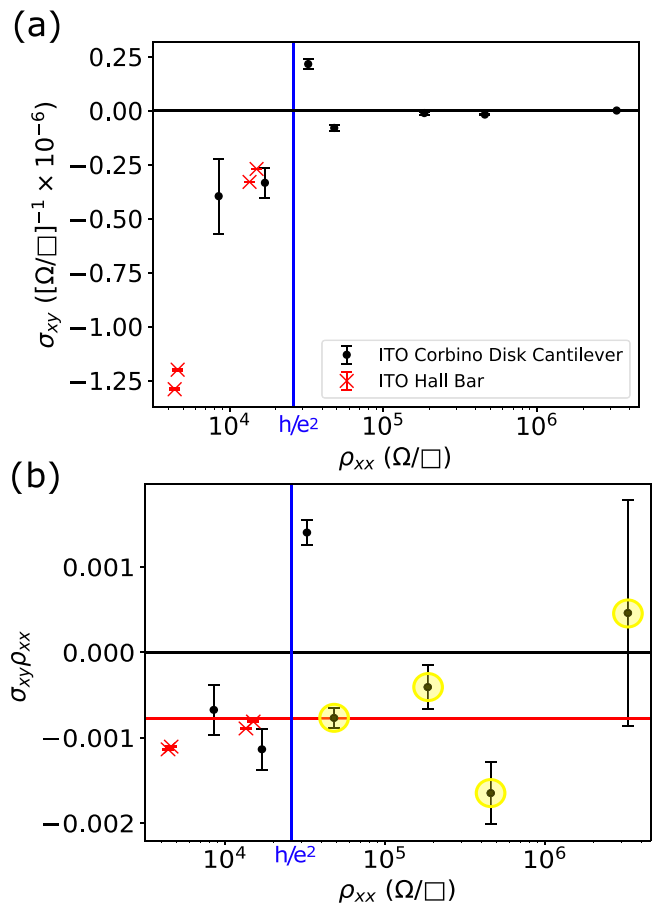

FIG. 4. Behavior of σ_{xy} and $\sigma_{xy}\rho_{xx}$ at 5 T measured on a series of annealed ITO samples through the MIT. The outlying sample very close to the MIT may be strongly influenced by the magnetic behavior as discussed in Secs. III B 2 and III B 3. Additional data obtained through a Hall bar approach and discussed in Sec. III C are included as a reference. Resistive and nonmagnetic points above the MIT are highlighted in (b).

on the order of temperature and frequency limits taken in the DC limit of the Hall resistivity. Similarly, it was emphasized in [42] that if both ρ_{xy} and ρ_{xx} are calculated and averaged over the disorder, they should both show divergence, while if the respective conductivities are averaged over the disorder the calculated ρ_{xy} may approach a constant. We directly measure σ_{xy} and σ_{xx}, which is a hybrid of the above two procedures.

We show $\sigma_{xy}\rho_{xx}$ in Fig. 4(b) to test the Hall behavior. The observed $\sigma_{xy}\rho_{xx}$ is approximately a constant, excluding the very vicinity of the MIT. Far above the MIT weak localization corrections may alter the ratio [47] at a level lower than the resolution of the experiment. However, on the insulating side, a Hall insulating behavior would require that $\sigma_{xy}\rho_{xx} \sim \rho_{xx}^{-1}$ in contrast to the observed behavior. A constant $\sigma_{xy}\rho_{xx}$ supports that in ITO above the MIT $\rho_{xy} \propto \rho_{xx}$. Such behavior would be expected if ρ_{xx} and ρ_{xy} both diverge as $1/n$ for thermally activated carrier density n as $T \to 0$.

2. Magnetism near the MIT

Successive annealing of highly insulating ITO resulted in increased granularity, lower resistivity, and the emergence of

TABLE II. Hysteretic magnetization fit coefficients obtained through torque magnetometry. Magnetization was more pronounced as B_s increased with increased annealing and lower resistance.

Resistivity ($k\Omega/\square$)	B_S (T)	α (mHz/T^2)
32	3 ± 0.1	3.6 ± 0.7
17	3.6 ± 0.1	5.4 ± 0.5
8.5	6 ± 0.2	3.1 ± 0.3

ferromagnetism as the MIT was approached. We now profile the origin of the surprising magnetism, as well as its anisotropy and dependence on the film morphology, carrier density, and defect density.

Anisotropy in bulk magnetization may be observed through cantilever torque magnetometry [33–36]. Hysteresis in magnetization due to ferromagnetic ordering results in hysteresis in $\Delta f_0(B)$ observed through Eqs. (3) and (4). Ferromagnetic hysteresis in $\Delta f_0(B)$ appeared after annealing near the MIT point as shown in Fig. 5. All tested cantilevers with patterned metallic layers displayed low-field shifts in f_0 as discussed in Appendix B, thus only the hysteresis in magnetization for $|B| > 1.5$ T can be attributed to sample magnetization. The amplitude of the magnetic hysteresis loop increased with annealing and confirms that the observed Δf_0 hysteresis arose from changes in the ITO. To rule out systematic factors, the order of data-taking was switched between the two 32-$k\Omega/\square$ data sets, and a 6-h delay at $+7$ T was inserted between the sweep-up and the sweep-down runs of the 17 $k\Omega/\square$ data set. The lack of hysteresis at a high magnetic field confirms that hysteresis in $\Delta f_0(B)$ arose from changes in the ITO instead of systematic factors. No hysteresis in magnetization was found for ITO with a sheet resistance >32 $k\Omega/\square$.

Magnetization hysteresis or hysteresis in Δf_0 above 1.5 T was fit to $\Delta f_{0,\text{hyst}} = \alpha(B - B_S)B$ for saturating field B_S and proportionality constant α. Fit coefficients are provided in Table II. The amplitude of magnetization and B_S increased with annealing, as previously observed in ITO [16]. Note that stronger z-axis magnetism increases f_0, while in-plane magnetism can decrease f_0. The lower f_0 during the ramp-down in magnetic field is thus consistent with in-plane ferromagnetism. In-plane ferromagnetism has been observed previously in ITO and a $B_s \approx 2$ T for the more lightly annealed samples is consistent with previous observations of ferromagnetic ITO at room temperature [5]. However, the coercive field of ITO can vary between samples by a factor of ≈ 10 [5,16,17] and increases with annealing.

The most annealed 8.5-$k\Omega/\square$ sample displayed a hysteretic magnetization saturating at $\Delta m \approx 0.002\mu_B/\text{f.u.}$, where f.u. is the In_2O_3 unit cell volume. If we assume that the associated moment with each defect is of order $\sim 1\mu_B$, we obtain an approximate magnetic defect density of 1.3×10^{19} defects/cm^3, within a factor of 2 of the carrier density listed in Table I. However, the large anisotropy field, the presence of magnetism in thin films and nanoparticles of ITO and other oxides which is absent in the bulk [11], and the annealing dependence of magnetism suggest [16] that the relevant magnetic properties are derived from the sample surface [11].
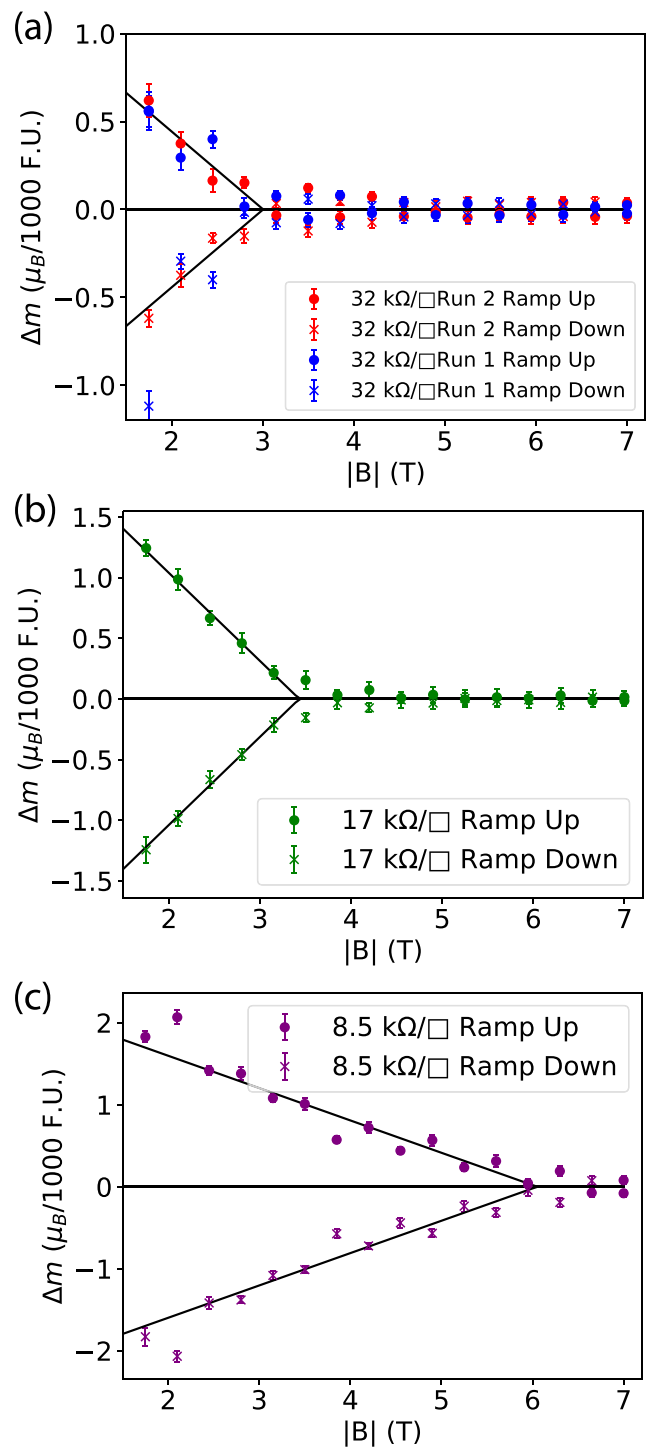

FIG. 5. Hysteresis in magnetization Δm for three annealed ITO resistivities. We calculate the hysteretic magnetic moment per "formula unit" (f.u.), approximated as the unit cell volume of crystalline In_2O_3. The amplitude of the hysteresis and saturating field increase with longer annealing as reported in Table II. Ramping of the magnetic field to ± 7 T was performed in 0.7-T steps.

Oxide surface vacancy-based magnetism could be enhanced by the granular transition shown in Fig. 3. If we distribute the moments only at the surface of the film and assume that, because of surface roughness the effective surface area

is increased by a factor of 2, we obtain a surface magnetization of $\sim 0.1 \mu_B$/f.u. One of 10 unit cells at the surface introduces a magnetic moment if each surface defect produces $\sim 1 \mu_B$. Finally, the anisotropy energy K_u can be approximated from the saturation magnetization and field. The approximate $K_u = B_s \Delta m_s / 2 \approx 2 \times 10^4$ J/m^3 is about 10 times lower than a typical anisotropy energy of a thin film of polycrystalline ferromagnetic Fe$_3$O$_4$ of similar thickness [48].

3. Anomalous Hall conductivity near the MIT

The most direct demonstration of intrinsic ferromagnetism is the emergence of the anomalous Hall effect in the transverse channel. For a material with z component of magnetization M_z and coefficients a and b,

$$\sigma_{xy} = aB + bM_z \rightarrow \delta f_0(\pm V, B) \propto B^2 + \beta B M_z. \quad (7)$$

Using Corbino disk torque magnetometry, we can detect both the Hall and the anomalous Hall effects. However, unlike a standard Hall bar configuration, the sample is voltage biased and the transverse conductivity $\sigma_{xy}(B)$ is directly measured by the magnetic moment created by circulating Hall currents.

There is clear evidence of nonlinear σ_{xy} or the anomalous Hall effect in the even component of $\delta f_0(\pm V, B)$. The extracted and fit σ_{xy} from $\delta f_0(\pm V, B)$ is shown in Fig. 6. The even component of $\delta f_0(\pm V, B)$ is fit to Eq. (7) assuming a diamagnetic sigmoidal M_z with fit coefficients a and b,

$$M_z = \frac{a}{e^{(B_s - B)/b} + 1}, \quad (8)$$

appearing at the B_s listed in Table II. An in-plane ferromagnet in the out-of-plane field should exhibit $M_z = 0$ at $B_z = 0$. The initial in-plane magnetization cants to the z axis as B_z increases and saturates at $B_z > B_s$. A sigmoidal M_z with $B_s \gg b$ replicates this behavior while minimizing free fit parameters. The anomalous Hall signal can be seen in Fig. 6 in both the agreement with the fit form of Eq. (7) and the fact that a linear extrapolation of the high-field σ_{xy} does not intersect $\sigma_{xy} = 0$ at $B = 0$. This is in contrast with the linear σ_{xy} shown in Fig. 2. Finally, the region of varying anomalous Hall signal corresponds with the hysteresis loop bounds shown in Fig. 5 as expected.

We further comment on the sign change of the 32-kΩ/$\square$ sample Hall conductivity shown in Fig. 6(a). Here we note that this sample was close to but on the insulating side of the MIT and thus at the onset of the hopping regime. A sign change of the anomalous Hall effect is then possible as a function of the impurity band filling [23]. As our films experienced strong variations in oxygen vacancies and defects as the morphology changed through annealing, such an effect may be anticipated. Indeed, such a sign reversal was previously observed in (In$_{0.27}$Co$_{0.73}$)$_2$O$_{3-v}$ (v denotes the oxygen vacancies) ferromagnetic semiconductors [49] in the variable-range hopping regime, particularly as the temperature was reduced and localization effects dominated. As materials like ITO are based on the In$_2$O$_3$ oxide system where oxygen vacancies and morphology contribute to the creation of the impurity band,
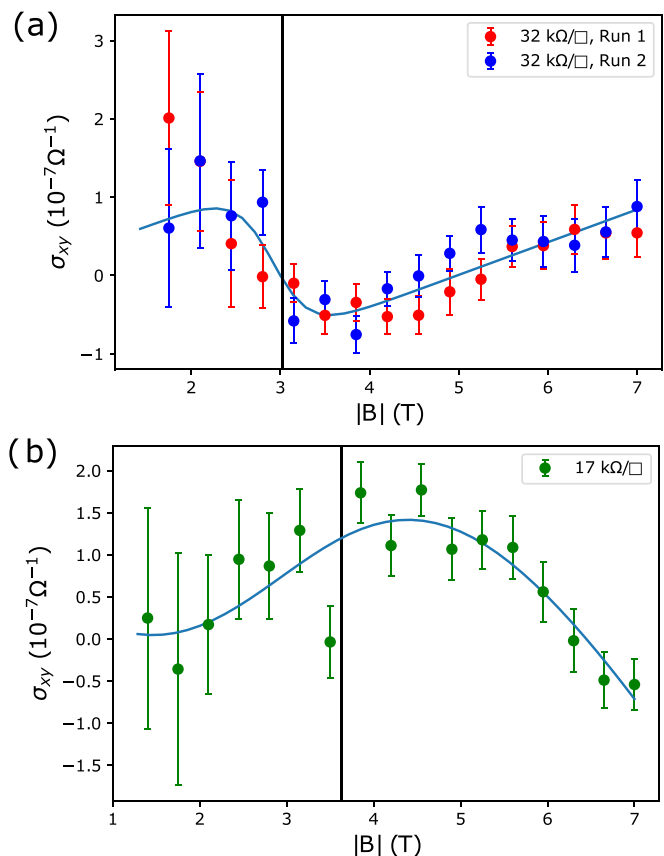

FIG. 6. Fits to the even component of $\delta f_0(\pm V, B)$ assuming a sigmoidal kink in the anomalous Hall signal at B_s. For comparison, B_s as fit from the closing of the Δf_0 hysteresis in Fig. 5 is shown by the vertical line. Low field cutoffs are imposed to avoid obscuring data with high error-bar points.

the sign change observed in our ITO samples may have the same origin.

4. Hysteretic transport

The detection of the AHE is also accompanied by hysteresis in $\delta f_0(\pm V, B)$. As shown in Fig. 7, there is a hysteretic component of $\delta f_0(\pm V, B)$, with peaks coinciding with the closing of the f_0 hysteresis loops. The smoothly varying nonhysteretic component of $\delta f_0(\pm V, B)$ is the average between the up and the down magnetic-field sweep values of $\delta f_0(\pm V, B)$ and is used to extract the Hall conductivity and magnetoresistance. The hysteretic component of $\delta f_0(\pm V, B)$ is the difference between the smoothly varying background and $\delta f_0(\pm V, B)$ in each sweep direction. Hysteresis in transport closes above B_S and qualitatively peaks near B_S for annealed magnetic ITO cantilever data sets. The hysteretic $\delta f_0(\pm V, B)$ is approximately 0 at low field, although such a closing may be due to the lack of dipole sensitivity at $B = 0$. While the hysteretic $\delta f_0(\pm V, B)$ signal cannot be simply ascribed to a single source, as both the magnetoresistance and the Hall conductivity have contributions from the sample magnetization, the fact that the hysteresis profile is not entirely even or odd in B suggests that both components are hysteretic. Finally, the $\delta f_0(\pm V, B)$ hysteresis coincided with
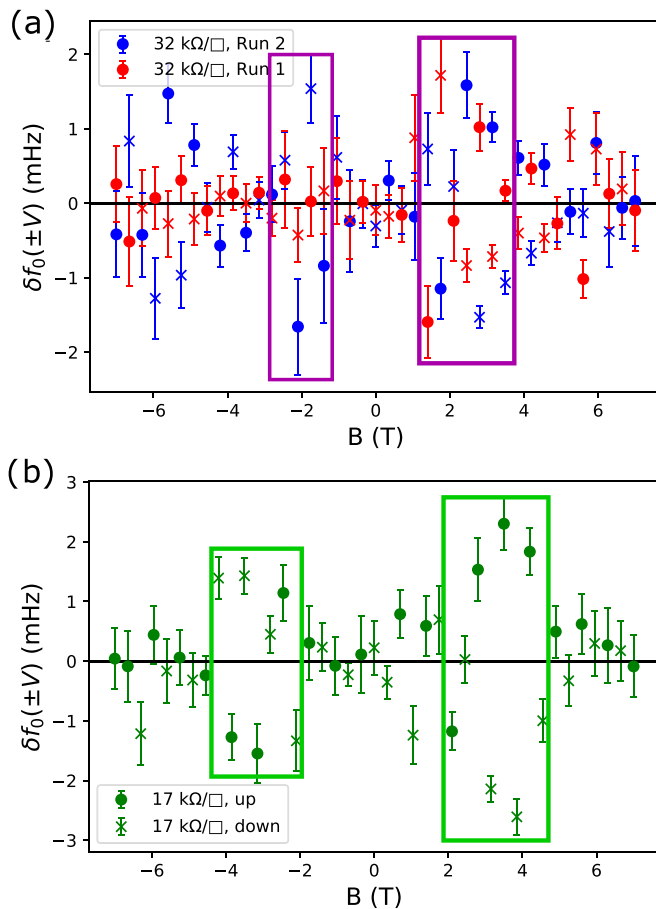
FIG. 7. Hysteresis in transport or $\delta f_0(\pm V, B)$ for 32- and 17-kΩ/□ annealed devices. Peaks near the closing of the hysteresis loops are highlighted in boxes. The Corbino disk voltage was ± 0.3 V. Hysteresis could appear due to both the magnetoresistance for $B \lesssim B_s$ and the anomalous Hall effect as $B \approx B_s$.

the hysteresis in magnetization and its evolution with annealing, confirming that both the transport and the magnetization hysteresis originate from the ITO.

C. ITO Hall bar transport

To confirm our findings using Corbino disk torque magnetometry and highlight the power of the technique, we performed complementary measurements using a standard Hall bar configuration. For a given temperature, the sample was current-biased on the x axis, and the longitudinal (x-axis) and transverse (y-axis) voltages were recorded as a function of the z-axis magnetic field. Detection of the anomalous Hall effect in the transverse channel in such a configuration is difficult due to sample issues such as the strong in-plane magnetic anisotropy and high sample resistance [15,19,20]. Negative magnetoresistance due to the reduction in spin-related scattering thus is typically used to relate transport to direct magnetization measurements in ITO. Hysteretic magnetoresistance would provide convincing evidence of ferromagnetism, pointing to the presence of magnetic domains that need to be flipped in direction when the magnetic field is reversed.
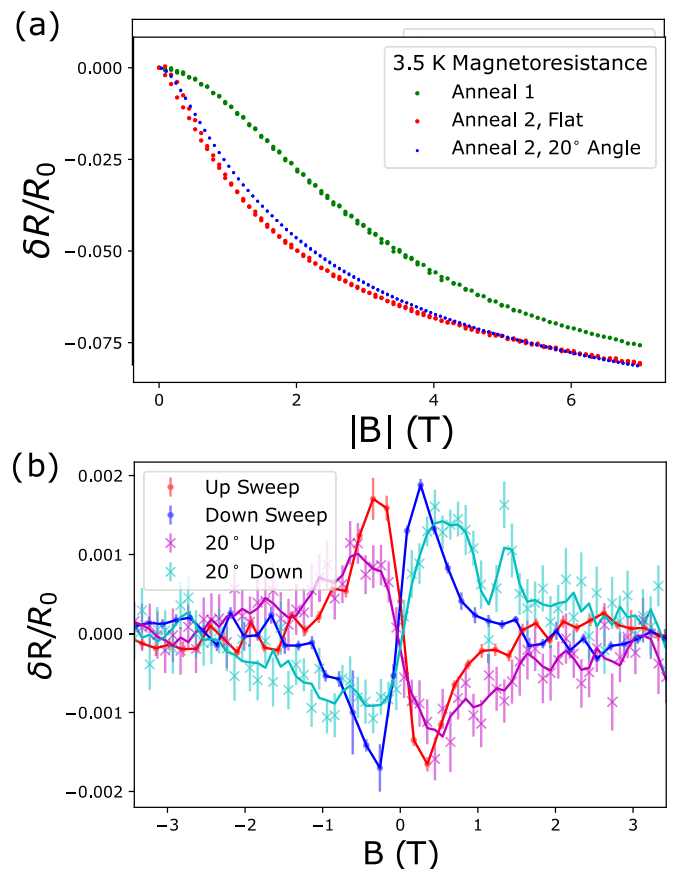

FIG. 8. (a) Magnetoresistance for a lightly annealed and a more strongly annealed ITO sample. (b) Hysteresis in magnetoresistance after two stages of annealing for a vertically and 20° mounted Hall bar.

Initially resistive ITO was sputtered in a Hall bar pattern and successively annealed to detect the onset of magnetism. Note that Hall bar measurements were performed on more conductive ITO films of the same thickness as the Corbino disk samples due to the difficulties in measuring high-resistance samples using a Hall bar technique. The $B = 0$ resistance was 15 kΩ/□ for the first anneal and 4.6 kΩ/□ for the second anneal. The relative magnetoresistance or $\delta R/R_0 \equiv [R(B) - R(0)]/R(0)$ for both anneals is shown in Fig. 8(a). More strongly annealed or conductive samples displayed more dramatic decreases in $\delta R/R_0$ at $|B| < 2$ T and asymptotic $\delta R/R_0$ at $|B| > 5$ T. The change in magnetoresistance to 7 T was $\approx -8\%$ for both annealed samples. The amplitude and shape of the magnetoresistance curves are consistent with those in previous studies of ITO with changing carrier density and temperature [50]. The resistivity and carrier density of the Hall bar samples are included in Table I.

Hall effect and magnetoresistance data were further examined for evidence magnetism. Hysteretic magnetoresistance was found by comparing $\delta R/R_0$ during a magnetic-field sweep up from -7 T to $+7$ T and sweep down from $+7$ T to -7 T. The average $\delta R/R_0$ during the up and down sweeps was then subtracted from each sweep $\delta R/R_0$ data set to produce Fig. 8(b). Hysteretic magnetoresistance was observed below 2 T after annealing. The sign of hysteresis is consistent with
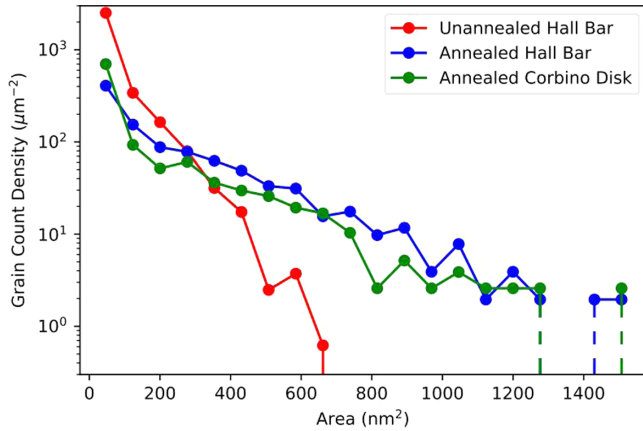
FIG. 9. Comparison of the grain sizes between annealed and nonannealed ITO samples by SEM. Fluctuations in SEM brightness changed from local noise to distinct larger grains with annealing.

previously observed in-plane magnetic ordering [5,16,51] and appeared only with annealing or increased granularity and carrier density. No hysteretic magnetoresistance was observed in the more lightly annealed data set, likely due to either increased magnetism with annealing or a lower slope in $\delta R/R_0$ near $B = 0$. No discernible anomalous Hall contribution could be detected, and the absence of the AHE is consistent with strong in-plane magnetic anisotropy.

The Corbino disk cantilevers exhibit a higher B_s than the hysteresis-closing B in the Hall bar samples shown in Fig. 8(b). The hysteresis closing field observed in the more annealed Hall bar ITO sample is approximately 2 T, while all Corbino disk B_s values are >3 T. Although magnetism is correlated with changes in granularity, after annealing there is no discernible difference in sample granularity between SEM images of the Hall bar and Corbino disk samples as shown in Fig. 9. Differences in sample microstructure thus do not explain the change in B_s between sample geometries. Cantilever angle and strong B_s anisotropy similarly do not account for differences in B_s. The applied B for ITO on Corbino disk cantilevers includes an in-plane B component due to cantilever bending. The ITO Hall bar was rotated by 20° from flat around the x axis, where current is applied in the x direction, to test for a strong in-plane field effect in B_s and simulate a cantilever angle. The 20° angle magnetoresistance and hysteretic magnetoresistance data are included in Fig. 8. Any changes in $\delta R/R_0$ and B_s with mounting angle were minimal and could be explained by slight differences in annealing between the flat and the angle-mounted Hall bars. The difference in B_s between the Corbino disk and the Hall bar samples thus is not caused by an in-plane magnetic field with cantilever bending. The observed closing of the hysteresis loop in $\delta R/R_0$ at 2 T may instead result from the lower dR/dB above 2 T. The hysteretic contribution to $\delta R/R_0$ from an effective offset in B between the up and the down magnetic-field sweeps is proportional to dR/dB. The magnetic field at which the hysteresis loop in Fig. 8(b) closes corresponds to a decrease in the slope of dR/dB in Fig. 8(a). Similarly, there was no observed hysteresis in the less annealed sample with a lower slope in $\delta R/R_0$ near $B = 0$.

The high-field slope in dR/dB therefore may not be high enough to observe hysteresis. The 2-T observed hysteresis loop closing field thus serves as a lower bound for B_s in the Hall bar, with more direct measurements found through torque magnetometry.

IV. CONCLUSIONS

We have shown unambiguous evidence of in-plane ferromagnetism and its effect on the transport properties of low-carrier-density ITO annealed through its MIT. Using a novel Corbino disk torque magnetometry technique [32], hysteresis in the voltage-independent shift in f_0 with B provides a direct measurement of in-plane magnetic ordering, while at a finite voltage $\delta f_0(\pm V, B)$ exhibits the AHE and hysteretic transport. In particular, the observation of the AHE provides direct evidence of inherent magnetism in ITO. Examination of both the Hall and the anomalous Hall contributions to $\delta f_0(\pm V, B)$ confirm the breaking of an in-plane magnetic ordering. Magnetism arose with annealing in ITO and thus with changes to the magnetic oxide morphology. The observation of intrinsic magnetism in ITO correlated with changes in surface morphology supports the hypothesis that magnetism arises from surface oxygen vacancies. Such Hall and magnetization measurements may be performed for deeply insulating materials due to the direct measurement of σ_{xy}. Initial results for σ_{xy} in resistive ITO contradict expectations for both a Hall insulator and standard models of Mott variable-range hopping [52–54]. Additionally, Corbino disk torque magnetometry provides the ability to simultaneously measure the bulk magnetic and transport properties of a material across the MIT, opening avenues for new physics.
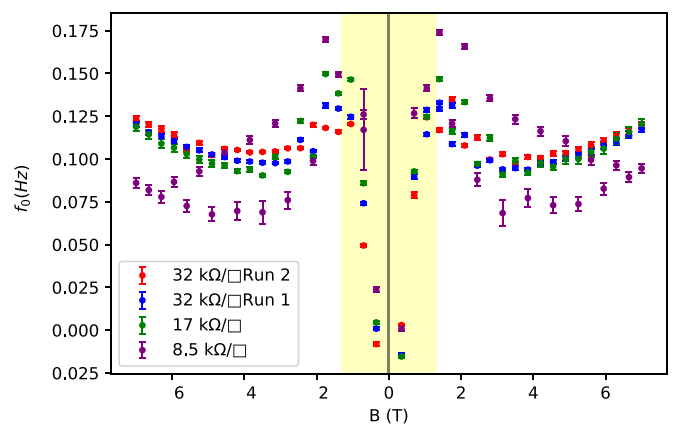
FIG. 10. Voltage-independent Δf_0 for four cooldowns. There is a rapid increase in Δf_0 in the yellow-shaded region of B near 0 T seen in all cooldowns regardless of the sample magnetization. The low-field Δf_0 is therefore not attributed to the ITO and is not fit in Fig. 5.

Yacoby and by the Department of Energy, Office of Science, Basic Energy Sciences, Materials Sciences and Engineering Division, under Contract No. DEAC02-76SF00515.

APPENDIX A: GRAIN ANALYSIS

A comparison of the unannealed and annealed grain structures observed by SEM in Fig. 3 is shown in Fig. 9. Grains were identified by adaptive thresholding of the SEM images. The unannealed Hall bar shows evidence of only SEM noise, which appears as very small grains. With further annealing,

regular granularity is observed. The granularity of the Hall bar and Corbino disk samples also become more similar after similar annealing treatment.

APPENDIX B: LOW-FIELD f_0 DEPENDENCE

The full profile of Δf_0 with magnetic field for four annealing strengths is shown in Fig. 10. Hysteresis appears as fluctuations in Δf_0 between neighboring B points when both sweep directions are plotted together. Without subtracting the background change in f_0 such hysteresis is clearest in the 8.5-kΩ sample.

[1] Y. Matsumoto, M. Murakami, T. Shono, T. Hasegawa, T. Fukumura, M. Kawasaki, P. Ahmet, T. Chikyow, S. ya Koshihara, and H. Koinuma, Room-temperature ferromagnetism in transparent transition metal-doped titanium dioxide, Science **291**, 854 (2001).

[2] S. B. Ogale, R. J. Choudhary, J. P. Buban, S. E. Lofland, S. R. Shinde, S. N. Kale, V. N. Kulkarni, J. Higgins, C. Lanci, J. R. Simpson, N. D. Browning, S. Das Sarma, H. D. Drew, R. L. Greene, and T. Venkatesan, High Temperature Ferromagnetism with a Giant Magnetic Moment in Transparent Co-Doped SnO$_{2-\delta}$, Phys. Rev. Lett. **91**, 077205 (2003).

[3] P. Sharma, A. Gupta, K. V. Rao, F. J. Owens, R. Sharma, R. Ahuja, J. M. O. Guillen, B. Johansson, and G. A. Gehring, Ferromagnetism above room temperature in bulk and transparent thin films of Mn-doped ZnO, Nat. Mater. **2**, 673 (2003).

[4] A. Tiwari, V. M. Bhosle, S. Ramachandran, N. Sudhakar, J. Narayan, S. Budak, and A. Gupta, Ferromagnetism in Co doped CeO$_2$: Observation of a giant magnetic moment with a high Curie temperature, Appl. Phys. Lett. **88**, 142511 (2006).

[5] N. H. Hong, J. Sakai, N. T. Huong, and V. Brizé, Room temperature ferromagnetism in laser ablated Ni-doped In$_2$O$_3$ thin films, Appl. Phys. Lett. **87**, 102505 (2005).

[6] G. Peleckis, X. Wang, and S. X. Dou, High temperature ferromagnetism in Ni-doped In$_2$O$_3$ and indium-tin oxide, Appl. Phys. Lett. **89**, 022501 (2006).

[7] O. D. Jayakumar, I. K. Gopalakrishnan, S. K. Kulshreshtha, A. Gupta, K. V. Rao, D. V. Louzguine-Luzgin, A. Inoue, P.-A. Glans, J.-H. Guo, K. Samanta, M. K. Singh, and R. S. Katiyar, Structural and magnetic properties of (In$_{1-x}$Fe$_x$)$_2$O$_3$ ($0.0 \leqslant x \leqslant .25$) system: Prepared by gel combustion method, Appl. Phys. Lett. **91**, 052504 (2007).

[8] C.-Y. Park, S.-G. Yoon, Y.-H. Jo, and S.-C. Shin, Room-temperature ferromagnetism observed in Mo-doped indium oxide films, Appl. Phys. Lett. **95**, 122502 (2009).

[9] M. Venkatesan, C. B. Fitzgerald, and J. M. D. Coey, Unexpected magnetism in a dielectric oxide, Nature (London) **430**, 630 (2004).

[10] N. H. Hong, J. Sakai, N. Poirot, and V. Brizé, Room-temperature ferromagnetism observed in undoped semiconducting and insulating oxide thin films, Phys. Rev. B **73**, 132404 (2006).

[11] A. Sundaresan, R. Bhargavi, N. Rangarajan, U. Siddesh, and C. N. R. Rao, Ferromagnetism as a universal feature of nanoparticles of the otherwise nonmagnetic oxides, Phys. Rev. B **74**, 161306(R) (2006).

[12] J. Philip, N. Theodoropoulou, G. Berera, J. S. Moodera, and B. Satpati, High-temperature ferromagnetism in manganese-doped indium-tin oxide films, Appl. Phys. Lett. **85**, 777 (2004).

[13] T. Ohno, T. Kawahara, H. Tanaka, T. Kawai, M. Oku, K. Okada, and S. Kohiki, Ferromagnetism in transparent thin films of Fe-doped indium tin oxide, Jpn. J. Appl. Phys. **45**, L957 (2006).

[14] M. Venkatesan, R. D. Gunning, P. Stamenov, and J. M. D. Coey, Room temperature ferromagnetism in Mn- and Fe-doped indium tin oxide thin films, J. Appl. Phys. **103**, 07D135 (2008).

[15] H. S. Kim, S. H. Ji, H. Kim, S.-K. Hong, D. Kim, Y. E. Ihm, and W. K. Choo, Observation of ferromagnetism and anomalous Hall effect in laser-deposited chromium-doped indium tin oxide films, Solid State Commun. **137**, 41 (2006).

[16] A. M. H. R. Hakimi, F. Schoofs, M. G. Blamire, S. Langridge, and S. S. Dhesi, Intrinsic and extrinsic ferromagnetism in Co-doped indium tin oxide revealed using x-ray magnetic circular dichroism, Adv. Condens. Matter Phys. **2017**, 2836254 (2017).

[17] H. S. Majumdar, S. Majumdar, D. Tobjörk, and R. Österbacka, Ferromagnetism in indium tin-oxide (ITO) electrodes at room temperature, Synth. Met. **160**, 303 (2010).

[18] J. M. D. Coey, P. Stamenov, R. D. Gunning, M. Venkatesan, and K. Paul, Ferromagnetism in defect-ridden oxides and related materials, New J. Phys. **12**, 053025 (2010).

[19] A. M. Hakimi, The quest for a dilute magnetic oxide, in *Magnetism and Spin Transport Studies on Indium Tin Oxide* (University of Cambridge, Cambridge, UK, 2011), pp. 63–96.

[20] J. Stankiewicz, F. Villuendas, and J. Bartolomé, Magnetic behavior of sputtered Co-doped indium-tin oxide films, Phys. Rev. B **75**, 235308 (2007).

[21] L. F. Arsenault, B. Movaghar, P. Desjardins, and A. Yelon, Magnetotransport in the insulating regime of Mn-doped GaAs, Phys. Rev. B **78**, 075202 (2008).

[22] M. A. Paalanen, S. Sachdev, R. N. Bhatt, and A. E. Ruckenstein, Spin Dynamics of Nearly Localized Electrons, Phys. Rev. Lett. **57**, 2061 (1986).

[23] A. A. Burkov and L. Balents, Anomalous Hall Effect in Ferromagnetic Semiconductors in the Hopping Transport Regime, Phys. Rev. Lett. **91**, 057202 (2003).

[24] N. M. Ahmed, F. A. Sabah, H. Abdulgafour, A. Alsadig, A. Sulieman, and M. Alkhoaryef, The effect of post annealing temperature on grain size of indium-tin-oxide for optical and electrical properties improvement, Results Phys. **13**, 102159 (2019).

[25] A. M. Hakimi, The indium oxide system, in *Magnetism and Spin Transport Studies on Indium Tin Oxide* (University of Cambridge, Cambridge, UK, 2011), pp. 41–60.

[26] S. Song, T. Yang, J. Liu, Y. Xin, Y. Li, and S. Han, Rapid thermal annealing of ITO films, Appl. Surf. Sci. **257**, 7061 (2011).

[27] J. H. Lee, Y. H. Kim, S. J. Ahn, T. H. Ha, and H. S. Kim, Grain-size effect on the electrical properties of nanocrystalline indium tin oxide thin films, Mater. Sci. Eng. B **199**, 37 (2015).

[28] L. Kerkache, A. Layadi, E. Dogheche, and D. Rémiens, Annealing effect in DC and RF sputtered ITO thin films, Eur. Phys. J. Appl. Phys. **39**, 1 (2007).

[29] D. Raoufi, A. Kiasatpour, H. Fallah, and A. Rozatian, Surface characterization and microstructure of ITO thin films at different annealing temperatures, Appl. Surf. Sci. **253**, 9085 (2007).

[30] M. Gulen, G. Yildirim, S. Bal, A. Varilci, I. Belenli, and M. Oz, Role of annealing temperature on microstructural and electro-optical properties of ITO films produced by sputtering, J. Mater. Sci.: Mater. Electron. **24**, 467 (2013).

[31] W.-F. Wu and B.-S. Chiou, Effect of annealing on electrical and optical properties of RF magnetron sputtered indium tin oxide films, Appl. Surf. Sci. **68**, 497 (1993).

[32] S. Mumford, T. Paul, S. H. Lee, A. Yacoby, and A. Kapitulnik, A cantilever torque magnetometry method for the measurement of Hall conductivity of highly resistive samples, Rev. Sci. Instrum. **91**, 045001 (2020).

[33] K. A. Modic, M. D. Bachmann, B. J. Ramshaw, F. Arnold, K. R. Shirer, A. Estry, J. B. Betts, N. J. Ghimire, E. D. Bauer, M. Schmidt, M. Baenitz, E. Svanidze, R. D. McDonald, A. Shekhter, and P. J. W. Moll, Resonant torsion magnetometry in anisotropic quantum materials, Nat. Commun. **9**, 3975 (2018).

[34] M. Perfetti, Cantilever torque magnetometry on coordination compounds: From theory to experiments, Coord. Chem. Rev. **348**, 171 (2017).

[35] J. Chiaverini, K. Yasumura, and A. Kapitulnik, Microcantilever studies of angular field dependence of vortex dynamics in $Bi_2 Sr_2 CaCu_2 O_{8-x}$, Phys. Rev. B **64**, 014516 (2001).

[36] A. C. Bleszynski-Jayich, W. E. Shanks, B. Peaudecerf, E. Ginossar, F. von Oppen, L. Glazman, and J. G. E. Harris, Persistent currents in normal metal rings Science **326**, 272 (2009).

[37] E. Finot, A. Passian, and T. Thundat, Measurement of mechanical properties of cantilever shaped materials, Sensors **8**, 3497 (2008).

[38] O. M. Von Corbino, Electromagnetic effects due to distortions that a field produces on nonmetallic ion paths, Phys. Z. **12**, 561 (1911).

[39] N. Manavizadeh, F. A. Boroumand, E. Asl-Soleimani, F. Raissi, S. Bagherzadeh, A. Khodayari, and M. A. Rasouli, Influence of substrates on the structural and morphological properties of RF sputtered ITO thin films for photovoltaic application, Thin Solid Films **517**, 2324 (2009).

[40] L. Friedman and M. Pollak, The Hall effect in the variable-range-hopping regime, Philos. Mag. B **44**, 487 (1981).

[41] T. Holstein, Studies of polaron motion: Part II. The "small" polaron, Ann. Phys. (NY) **8**, 343 (1959).

[42] O. Entin-Wohlman, A. G. Aronov, Y. Levinson, and Y. Imry, Hall Resistance in the Hopping Regime: A "Hall Insulator"?, Phys. Rev. Lett. **75**, 4094 (1995).

[43] O. Viehweger and K. B. Efetov, Low-frequency behavior of the kinetic coefficients in localization regimes in strong magnetic fields, Phys. Rev. B **44**, 1168 (1991).

[44] S. Kivelson, D.-H. Lee, and S.-C. Zhang, Global phase diagram in the quantum Hall effect, Phys. Rev. B **46**, 2223 (1992).

[45] Y. Imry, Zero-Temperature Frequency-Dependent Hall Conductivity of the Anderson Insulator, Phys. Rev. Lett. **71**, 1868 (1993).

[46] P. F. Hopkins, M. J. Burns, A. J. Rimberg, and R. M. Westervelt, Magnetic-field-induced localization in degenerately doped n-type Ge, Phys. Rev. B **39**, 12708 (1989).

[47] D. W. Koon and T. G. Castner, Hall effect near the metal-insulator transition, Phys. Rev. B **41**, 12054 (1990).

[48] E. Liu, Z. Huang, J.-G. Zheng, J. Yue, L. Chen, X. Wu, Y. Sui, Y. Zhai, S. Tang, J. Du, and H. Zhai, Texture induced magnetic anisotropy in Fe_3O_4 films, Appl. Phys. Lett. **107**, 172403 (2015).

[49] R. M. Qiao, S. S. Yan, T. S. Xu, M. W. Zhao, Y. X. Chen, G. L. Liu, W. L. Yang, R. K. Zheng, and L. M. Mei, Anomalous Hall effect in variable range hopping regime: Unusual scaling law and sign reversal with temperature, arXiv:1406.5672.

[50] A. Fujimoto, K. Yoshida, T. Higaki, Y. Kimura, M. Nakamoto, Y. Kashiwagi, M. Yamamoto, M. Saitoh, T. Ohno, and S. Furuta, Negative magnetoresistance of indium tin oxide nanoparticle thin films grown by chemical thermolysis, J. Phys. Soc. Jpn. **82**, 024710 (2013).

[51] M. Majumder, M. Schmidt, H. Rosner, A. A. Tsirlin, H. Yasuoka, and M. Baenitz, Anisotropic Ru^{3+} $4d^5$ magnetism in the alpha-$RuCl_3$ honeycomb system: Susceptibility, specific heat, and zero-field NMR, Phys. Rev. B **91**, 180401(R) (2015).

[52] R. Németh and B. Mühlschlegel, Hopping Hall conductivity in disordered and granular systems, Solid State Commun. **66**, 999 (1988).

[53] D. Koon and T. Castner, Variable-range hopping and the Hall coefficient in Si:As, Solid State Commun. **64**, 11 (1987).

[54] M. Gruenewald, H. Mueller, P. Thomas, and D. Wuertz, The hopping Hall mobility—A percolation approach, Solid State Commun. **38**, 1011 (1981).

Correction: A byline footnote and indicator for the second author were inadvertently removed during the production cycle and have now been reinserted.